Confinement and ELM characteristics of H-mode plasmas in KSTAR

2012 Nucl. Fusion 52 114001

(http://iopscience.iop.org/0029-5515/52/11/114001)

IOP Publishing and International Atomic Energy Agency | Nuclear Fusion

Nucl. Fusion **52** (2012) 114001 (12pp) doi:10.1088/0029-5515/52/11/114001

Confinement and ELM characteristics of H-mode plasmas in KSTAR

J-W. Ahn,[1,a], H.-S. Kim[2], Y.S. Park[3], L. Terzolo[4], W.H. Ko[4], J.-K. Park[5], A.C. England[4], S.W. Yoon[4], Y.M. Jeon[4], S.A. Sabbagh[3], Y.S. Bae[4], J.G. Bak[4], S.H. Hahn[4], D.L. Hillis[1], J. Kim[4], W.C. Kim[4], J.G. Kwak[4], K.D. Lee[4], Y.S. Na[2], Y.U. Nam[4], Y.K. Oh[4] and S.I. Park[4]

[1] Oak Ridge National Laboratory, Oak Ridge, TN 37831, USA
[2] Department of Nuclear Engineering, Seoul National University, Seoul 151-742, Korea
[3] Department of Applied Physics and Applied Mathematics, Columbia University, New York, NY 10027, USA
[4] National Fusion Research Institute, Daejeon 305-333, Korea
[5] Princeton Plasma Physics Laboratory, Princeton, NJ 08543, USA

E-mail: jahn@pppl.gov

Received 22 March 2012, accepted for publication 15 August 2012
Published 2 October 2012
Online at stacks.iop.org/NF/52/114001

Abstract

The latest results of confinement and edge-localized mode (ELM) characteristics of Korea Superconducting Tokamak Advanced Research (KSTAR) H-mode plasmas are reported. The estimation of fast ion contribution to the total stored energy, calculated by both the NUBEAM and ASTRA simulations, and of the effective total heating power is used to derive the thermal energy confinement time ($\tau_{E,\mathrm{thermal}}$), which is compared with a multi-machine database. The measured power threshold for the L–H transition (P_{thr}) as a function of density shows a roll-over with minimum value at $\bar{n}_e \sim 2 \times 10^{19}\,\mathrm{m}^{-3}$. KSTAR H-mode plasmas exhibit three distinctive types of ELMs: large type-I ELMs, intermediate ELMs and a mixed (type-I and small ELM peaks) ELM regime. Power scans show that the frequency of the large ELMs increases with increasing heating power, a feature of type-I ELMs. The quality of confinement is higher for type-I and mixed ELMy H-mode ($H_{98(y,2)} \sim 0.9$–1) than for the intermediate ELM regime ($H_{98(y,2)} \sim 0.7$). Type-I ELMs have precursor-like signals from the magnetics measurement, while the other two ELM types do not. The low-field side (LFS) profile of electron temperature (T_e), from the ECE measurement, and the pedestal profile of the toroidal velocity (V_t), from charge-exchange spectroscopy, show a continuous build up on the LFS during the inter-ELM period. However, the pedestal ion temperature (T_i) remains unchanged for most of the inter-ELM period until it rapidly rises in the last stage of the ELM cycle ($\geqslant$70–80%). The estimated electron pedestal collisionality for a type-I ELMy regime is $v_e^* \sim 0.5$–0.6. The confinement and ELM characteristics for the ELM suppression discharges by the application of an $n = 1$ magnetic perturbation (MP) have also been investigated for each of the identified stages during the MP application. A second L–H transition during the L-mode phase after the end of first H-mode stage occurs for some discharges when the divertor configuration is restored by the plasma control system. Characteristics of this late H-mode are compared with those for the main H-mode.

(Some figures may appear in colour only in the online journal)

1. Introduction

H-mode access and confinement characteristics are two of the important topics in fusion research and the present database needs to be projected to the future machines such as ITER. While the understanding of physical mechanisms responsible for the L–H transition and the H-mode pedestal phenomena with various types of edge-localized modes (ELMs) has advanced rapidly in recent years, a significant part of the fundamental physical processes is still to be examined and the suggested models to be tested in the present-day machines. Korea Superconducting Tokamak Advanced Research (KSTAR) [1, 2] is a superconducting, long-pulse tokamak with similar magnetic geometry to ITER and began operation in 2008. It obtained the first H-mode in 2010 with neutral beam injection (NBI) heating [3]. Even with rather fixed operation parameters and relatively low heating power ($I_p = 0.6$ MA, $B_t = 2$ T, $P_{\mathrm{NBI}} \leqslant 1.5$ MW), H-mode plasmas with multiple types of ELMs, including clear type-I ELMs

---

[a] Princeton Plasma Physics Laboratory, MS-15, Princeton, NJ 08543, USA.

and a mixed-ELM (type-I + small ELMs) regime, and different confinement qualities have been produced. Note that type-I ELMs in other machines are generally observed only when the heating power is well above the L–H power threshold (P_{thr}) [4]. One factor that appeared to have influenced ELMs in KSTAR is the shape of the poloidal plasma cross section. The shaping parameters are known to affect confinement and to change the ELM characteristics in other machines. A range of elongation (κ up to 1.8–1.9) and triangularity (δ up to 0.8–0.9) have been achieved and higher δ appears to lead to the mixed-ELM regime in KSTAR.

The measured P_{thr} in KSTAR [3] increases with decreasing $\bar{n}_{\mathrm{e}}$ (line average density, measured by a 280 GHz single-channel millimetre wave interferometer system [5]), for $\bar{n}_{\mathrm{e}} \leqslant 2 \times 10^{19}\,\mathrm{m}^{-3}$. Similar observations have been reported from several other machines [6, 7] while there are also examples [8, 9] of no such trend. The present P_{thr} scaling law [10] does not predict the 'roll-over' in the low-density regime and modelling for the L–H transition is still being developed to include this effect (for example, see [11]). The electron temperature (T_{e}), measured by ECE [12], and ion temperature (T_{i}), measured by charge-exchange spectroscopy (CES) [13], are higher in the core than are observed in other machines with similar sizes and heating power levels; $T_{\mathrm{e}0} = 3$–4 keV and $T_{\mathrm{i}0} = 2$–3 keV are readily available with only 1.5 MW NBI power and this suggests that the electron thermal transport is quite low in KSTAR. The momentum transport also appears to be low as the toroidal velocity (V_{t}) at the plasma centre reaches 150–200 km s^{-1} with $P_{\mathrm{NBI}} = 1.5$ MW. Although detailed profile measurements necessary for the ELM stability study are not routinely available at present, it is worthwhile to report phenomenological investigations of the ELM characteristics and global confinement properties in KSTAR and to compare the results with those from other machines. Also, the recent achievement of ELM suppression using an external $n = 1$ magnetic perturbation (MP) [14] motivates a study of its ELM and confinement characteristics to be launched, and the first set of observations is reported as a part of this paper. Figure 1 shows a time trace of several plasma parameters for a typical type-I ELMy H-mode plasma. Note that a second L–H transition later during the discharge occurred in this case, producing the 'late H-mode' which has different ELM and confinement characteristics from the preceding main H-mode.

A brief description of the experimental setup is given in section 2. Section 3 will describe conditions for the access to the H-mode, estimation of confinement time, and general characteristics of ELMs. Profile measurement results during the inter-ELM period for type-I ELMy H-mode are given in section 4. Section 5 is devoted to the confinement and ELM characteristics of ELM suppressed H-mode plasmas by the $n = 1$ MPs. The access condition and characteristics of late H-mode are reported in section 6, followed by a summary and discussion in section 7.

2. Experimental setup

In the 2011 campaign, H-mode plasmas were routinely obtained with the use of NBI ($0.7 \leqslant P_{\mathrm{NBI}} \leqslant 1.5$ MW). The electron cyclotron heating (ECH) with maximum power of ~0.3 MW for 110 GHz and ~0.6 MW for 170 GHz gyrotrons was also used as another primary heating method. Real-time EFIT (rtEFIT) was implemented as a part of the plasma control system but iso-flux control capability was not available and the magnetic configuration was only optimized with a pre-programmed waveform of poloidal field coil currents, i.e. the feedback control was not possible. The post-discharge EFIT equilibrium reconstruction was also implemented in good agreement with the CCD camera images for the plasma boundaries and the positions of strike points. Details of the equilibrium reconstruction process used in KSTAR can be found in [15]. Various wall cleaning techniques, including the plasma-facing component (PFC) baking up to ~250 °C, overnight helium glow discharge, and the PFC boronization using carborane, have been used to minimize impurity influx from the wall.

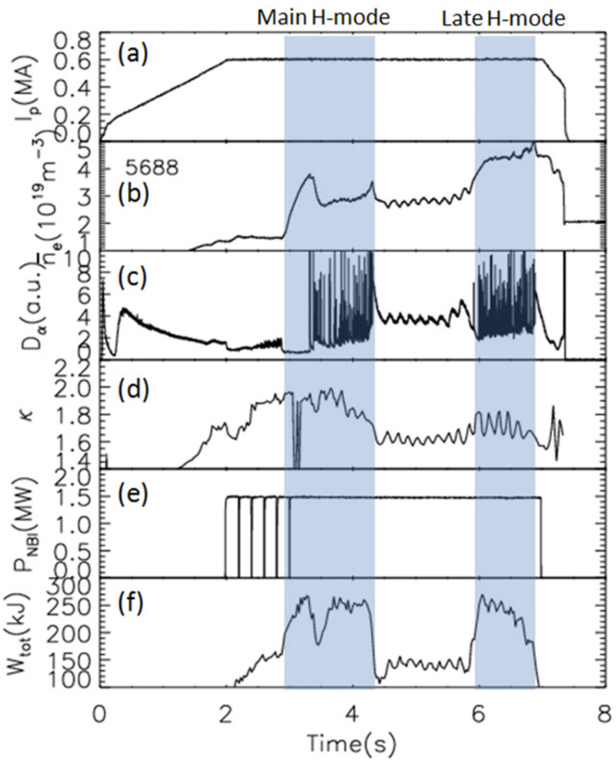

Figure 1. Time traces of (*a*) plasma current, (*b*) line average density, (*c*) mid-plane tangential D_α, (*d*) plasma elongation, (*e*) NBI heating power, and (*f*) total stored energy calculated by EFIT.

3. Access to the H-mode and general characteristics of ELMs

3.1. Dependence of P_{thr} on the density

There can be several definitions of the necessary power for access to the H-mode and we use the effective total heating power (P_{loss}) as described in the following equation:

$$P_{\mathrm{loss}} = P_{\mathrm{Ohm}} + P_{\mathrm{aux}}^{\mathrm{abs}} - \frac{\mathrm{d}W_{\mathrm{tot}}}{\mathrm{d}t}. \qquad (1)$$

Here, P_{Ohm} is the ohmic heating power and $P_{\mathrm{aux}}^{\mathrm{abs}}$ is the absorbed auxiliary heating power both for the NBI and ECRH, i.e. $P_{\mathrm{aux}}^{\mathrm{abs}} = P_{\mathrm{NBI}}^{\mathrm{abs}} + P_{\mathrm{ECRH}}^{\mathrm{abs}}$. The absorbed NBI power is computed by the NBI module [16] embedded in the Automatic System of Transport Analysis (ASTRA) [17] and NUBEAM [18, 19] codes, where $P_{\mathrm{NBI}}^{\mathrm{abs}} = P_{\mathrm{NBI}}^{\mathrm{inj}} - P_{\mathrm{NBI}}^{\mathrm{loss}}$ is used for the calculation. The NBI loss power $P_{\mathrm{NBI}}^{\mathrm{loss}}$ includes contributions from the orbit loss, charge exchange (CX), and the NBI shine through. On the other hand, the injected ECRH power is assumed to be absorbed into the plasma without any loss, i.e. $P_{\mathrm{ECRH}}^{\mathrm{abs}} = P_{\mathrm{ECRH}}^{\mathrm{inj}}$. KSTAR has no radiation power (P_{rad}) measurement at present and P_{rad} is not considered in the power balance equation in this work, following the convention in L–H power threshold studies [6–8, 10] and scaling laws for H-mode confinement [20] on other tokamak machines. W_{tot} is the total stored energy including contributions both from the thermal (W_{thermal}) and fast ion (W_{fast}) components and is calculated by EFIT.

A fine NBI power scan was carried out by changing the NBI duty cycle at each of the three density levels ($\bar{n}_e = 1.1, 1.7, 2.4 \times 10^{19}\,\mathrm{m}^{-3}$) in order to identify the threshold power for the L–H transition. P_{thr} values for other densities between these points were estimated by comparing a pair of discharges with and without the transition in a similar range of P_{loss} and $\bar{n}_e$, with all other parameters kept as constant as possible. The dataset reveals a minimum P_{thr} near $\bar{n}_e \sim 2 \times 10^{19}\,\mathrm{m}^{-3}$, i.e. the 'roll-over' of P_{thr} with $\bar{n}_e$ across the density range from $\sim 1.2 \times 10^{19}$ to $\sim 2.7 \times 10^{19}\,\mathrm{m}^{-3}$. The trend of P_{thr} below $\bar{n}_e \sim 2 \times 10^{19}\,\mathrm{m}^{-3}$ is similar to the result obtained in 2010 [3], which only showed the left branch with $\bar{n}_e$ lower than $\sim 2 \times 10^{19}\,\mathrm{m}^{-3}$. This result follows the trend observed in other machines [6, 7], although recent data from JET [8] and EAST [9] did not show the P_{thr} roll-over in the low-density regime. On the other hand, the present multi-machine database [10] for the extrapolation of P_{thr} to ITER (equation (2)) only has a strong positive dependence on the density and therefore does not predict this roll-over.

$$P_{\mathrm{thr,scaling}} = 0.0488 \pm 0.0028 n_{e20}^{0.717\pm0.035} B_{\mathrm{T}}^{0.803\pm0.032} \times S^{0.941\pm0.019}. \qquad (2)$$

Here, n_{e20} is the density in the unit of $10^{20}\,\mathrm{m}^{-3}$ and S is the plasma surface area in m. Figure 2 shows the plot of P_{thr} versus density for the results both from the 2010 and 2011 campaigns. The two datasets show good agreement in the lower density branch, i.e. below $\bar{n}_e \sim 2 \times 10^{19}\,\mathrm{m}^{-3}$, and data for 2011 indeed shows an increase in P_{thr} for $\bar{n}_e \geqslant 2 \times 10^{19}\,\mathrm{m}^{-3}$. Also overlaid is the power threshold predicted by the scaling law ($P_{\mathrm{thr,scaling}}$). Note that the discrepancy between the measured P_{thr} and the prediction from the scaling law becomes larger with decreasing density. For densities above $\bar{n}_e \sim 2 \times 10^{19}\,\mathrm{m}^{-3}$, the agreement between the measured and predicted P_{thr} is good, which indicates that the power threshold in KSTAR may follow the multi-machine scaling law for the higher density branch. We will continue to build up the power threshold database for a wider range of densities and P_{loss} in the upcoming campaign in late 2012.

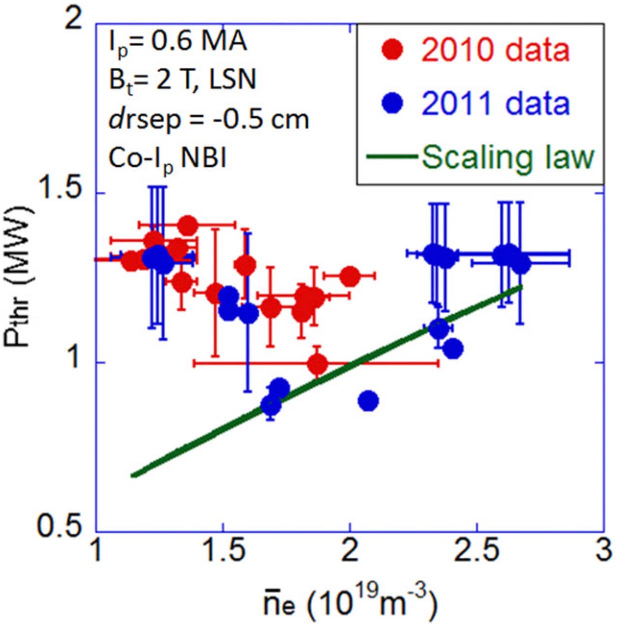

Figure 2. Measured L–H power threshold (P_{thr}) obtained during the experimental campaigns in 2010 (red) and 2011 (blue). Green line indicates the predicted P_{thr} from the multi-machine scaling law (equation (2)).

3.2. Estimation of τ_E and confinement quality

The plasma stored energy is a sum of thermal and fast ion contributions as was mentioned in the previous section. W_{fast} comes from the injected neutral beam particles through the CX process and can be estimated by NUBEAM or ASTRA simulation. The contribution is 10–35% of W_{tot} for the dataset in this study. This yields the thermal stored energy, $W_{\mathrm{thermal}} = W_{\mathrm{tot}} - W_{\mathrm{fast}}$, and enables us to estimate thermal energy confinement time $\tau_{E,\mathrm{thermal}} = W_{\mathrm{thermal}}/P_{\mathrm{loss}}$. The L–H transition in KSTAR usually occurs at a density below $\bar{n}_e \sim 2.5 \times 10^{19}\,\mathrm{m}^{-3}$ and therefore the effect of fast ion confinement can be particularly important. Figure 3 is an example of the ratio of W_{fast} to W_{tot}, calculated by NUBEAM and ASTRA, as a function of the line average density obtained from multiple discharges to cover a wide range of density. It is seen that the fraction of W_{fast} decreases stronger than linearly as the density increases from 1.3×10^{19} to $4.5 \times 10^{19}\,\mathrm{m}^{-3}$, which demonstrates the strong density dependence of fast ion contribution to the total stored energy. The beam slowing down time becomes shorter with higher density and therefore the NBI shine through and orbit loss decrease, leading to a reduced fraction of fast ion stored energy.

The estimated thermal energy confinement time is then compared with predictions by a multi-machine scaling law for the international database of energy confinement time, such as IPB98(y,2) [20] as follows,

$$\tau_{E,\mathrm{IPB98}(y,2)} = 0.0562 I_{\mathrm{p}}^{0.93} B_{\mathrm{T}}^{0.15} P^{-0.69} n^{0.41} M^{0.19} R^{1.39} \times \varepsilon^{0.58} \kappa^{0.78}, \qquad (3)$$

where I_{p} is in MA, P is the power (MW), n is the density ($10^{20}\,\mathrm{m}^{-3}$), M is the atomic mass, ε is the inverse aspect ratio and κ is the plasma elongation. Note that IPB98(y,2) is an H-mode scaling law for the thermal energy confinement time. The H-factor (energy confinement time normalized to the value predicted by the scaling law) indicates how good the confinement quality is compared with the multi-machine scaling law with various operation parameters taken into account. $H_{98(y,2)} = \tau_{E,\mathrm{thermal}}/\tau_{E,\mathrm{IPB98}(y,2)}$, is an indicator of the quality of the thermal energy confinement time and values of $H_{98(y,2)}$ higher than 1 mean that the experimentally obtained $\tau_{E,\mathrm{thermal}}$ is longer than the prediction of the IPB98(y,2)

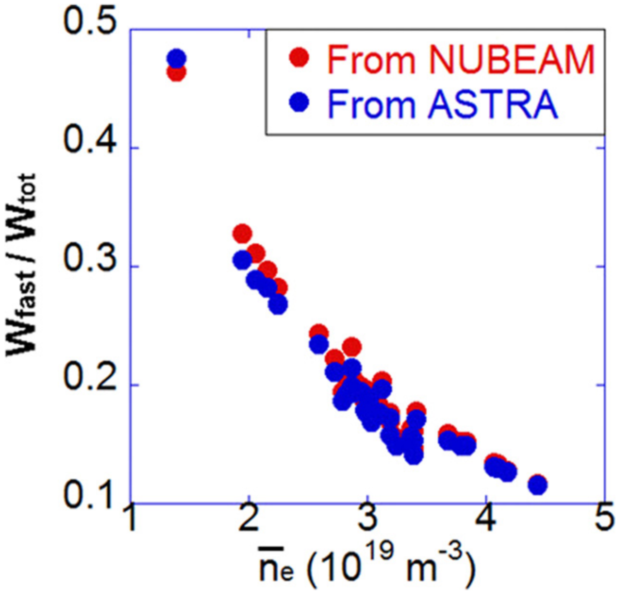

Figure 3. Density dependence of fast ion stored energy, normalized to the total stored energy, calculated by NUBEAM and ASTRA simulations. The data points were obtained from multiple discharges in order to cover a wide range of line average density.

scaling law. Accurate estimation of $H_{98(y,2)}$ therefore relies on accurate calculation of $W_{\rm fast}$, which becomes more important in the low-density regime because of the strong density dependence as shown in figure 3.

3.3. Characteristics of three types of ELMy H-mode

KSTAR H-mode plasmas exhibit three distinctive types of ELMs: (1) large type-I ELMs with low ELM frequency ($f_{\rm ELM}$ = 10–50 Hz) and good confinement ($H_{98(y,2)} = 0.9$–1), (2) intermediate, possibly type-III, ELMs with higher ELM frequency ($f_{\rm ELM}$ = 40–250 Hz) and poorer confinement ($H_{98(y,2)} = 0.6$–0.8), and (3) a mixed, large type-I and tiny peaks, ELM regime with good confinement ($H_{98(y,2)} \sim 1$). Figure 4 shows time traces of relevant parameters for all three types of ELMs.

Although the maximum NBI heating power was only 1.5 MW, many of the KSTAR ELMs showed characteristics of type-I ELMs (see figure 4(*a*)) including low ELM frequency, large ELM size (up to ~4% of $\Delta\bar{n}_{\rm e}/\bar{n}_{\rm e}$ and ~7% of $\Delta W_{\rm tot}/W_{\rm tot}$), and particularly the positive dependence of the ELM frequency on the heating power, i.e. increasing $f_{\rm ELM}$ with increasing power, according to the characterization in [21], confirmed experimentally in [4]. Figure 5 shows an example of the two power levels (1.5 MW and 1.3 MW of $P_{\rm NBI}$) and the ELM frequency is consistently higher for the 1.5 MW case. The outliers at $f_{\rm ELM}$ = 30–50 Hz in figure 5 represent the secondary ELM peaks adjacent to the primary ELM bursts. The ELM frequency for a specific ELM peak is calculated as the reciprocal of the time interval from the immediately preceding ELM peak. Therefore, the secondary ELM peaks always have higher $f_{\rm ELM}$ than the primary ELMs but this does not reflect the characteristics of the primary ELMs. Thus one only has to pay attention to the relationship of $f_{\rm ELM}$ for the primary ELMs with the heating power. Figure 6 shows an example of a power scan for the mixed-ELM regime (see figure 4(*c*)) by means of beam modulation and ECH injection. The NBI duty cycle was changed during the discharge in order to reduce the injected power from 1.5 to 1.1 MW for the period of t = 2.5–3.5 s. In addition, 0.4 MW of ECH power was injected for t = 3–3.5 s, making the total injected power for this period similar to the level before the NBI modulation. It is seen that the frequency of large ELM peaks decreases from $t \sim 2.65$ s for the lower NBI power stage ($P_{\rm NBI}$ = 1.1 MW) and it lasts until $t \sim 3.15$ s before it increases again when the total injected power rises back up to 1.5 MW by the addition of ECH power. Note that there is a time delay of ~150 ms in the response of the ELM frequency to the change in the injected power at t = 3 s, which is consistent with the beam slowing down time of 100–150 ms estimated for the given beam energy and plasma conditions. The time delay of ~200 ms in the ELM frequency response at t = 4 s could be explained by the energy confinement time scale of ~200 ms. These data suggest that large ELM peaks either in the category 1 or 3 mentioned in the previous paragraph may be in the type-I ELMy regime even with the relatively lower power level ($P_{\rm NBI} + P_{\rm ECH}$ = 1.1–1.5 MW). When the heating power is so close to the L–H power threshold, tokamaks usually observe the occurrence of type-III ELMs with higher $f_{\rm ELM}$ and smaller ELM size [4]; a transition to the larger type-I ELMy regime usually follows with increased heating power. Thus our categorization as type-I ELMs should be considered preliminary, to be confirmed with the greater heating power to be available in the coming sets of experiments. In addition, figure 6 also shows that there are tiny ELMs between large type-I ELM peaks. The plasma therefore appears to be in a mixed-ELM regime, with resistive ELMs mixed in with the ideal ones. These small ELMs usually cause a density loss of only 0.5% or less.

The intermediate ELMs (see figure 4(*b*)) have different characteristics from those for the other two types of ELMs. Results from other machines indicate that the ELM size defined as a pedestal energy loss ($\Delta W_{\rm ELM}/W_{\rm ped}$) has a negative dependence on the Greenwald fraction ($\bar{n}_{\rm e}/n_{\rm G}$) for type-I ELMs [22, 23] but currently there is no routine measurement of pedestal $T_{\rm e}$ and $n_{\rm e}$ profiles in KSTAR, therefore we use $\Delta\bar{n}_{\rm e}/\bar{n}_{\rm e}$ to look for the ELM size dependence on $\bar{n}_{\rm e}/n_{\rm G}$. Figures 7(*a*) and (*b*) show that the size of type-I ELMs decreases with increasing ELM frequency and the Greenwald fraction, while the size of the intermediate ELMs does not show a clear correlation with either $f_{\rm ELM}$ or $\bar{n}_{\rm e}/n_{\rm G}$ (both type-I and intermediate ELM data were obtained from multiple discharges). The size of the intermediate ELMs is $\Delta\bar{n}_{\rm e}/\bar{n}_{\rm e} < 2\%$ in figure 7 and even smaller than 1% in some other discharges. Figure 7(*c*) shows the variation of $H_{98(y,2)}$ for type-I and intermediate ELMs as a function of the Greenwald fraction. It is seen that the confinement degrades with increasing density for both types of ELMs and the overall H-factor for the intermediate ELMs is noticeably lower than for type-I ELMs. This indicates that the intermediate ELMs might be type-III and it is consistent with its higher ELM frequency and smaller ELM size. However, power scan data and the relation with the ELM frequency are necessary to confirm this.

We have also carried out a wavelet analysis of the Mirnov signals and found that type-I ELMs usually have an increased fluctuation level in the low-frequency band (25–50 kHz) during

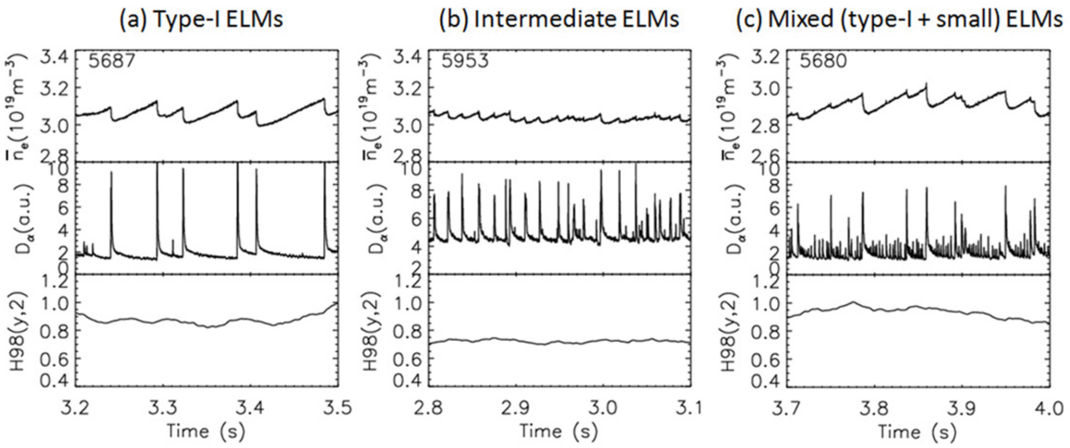

Figure 4. Time traces of line average density (upper), D_α intensity (middle) and H_{98}-factor (lower) for three identified types of ELMs; (*a*) large type-I ELMs, (*b*) intermediate ELMs and (*c*) mixed (type-I + small) ELMs.

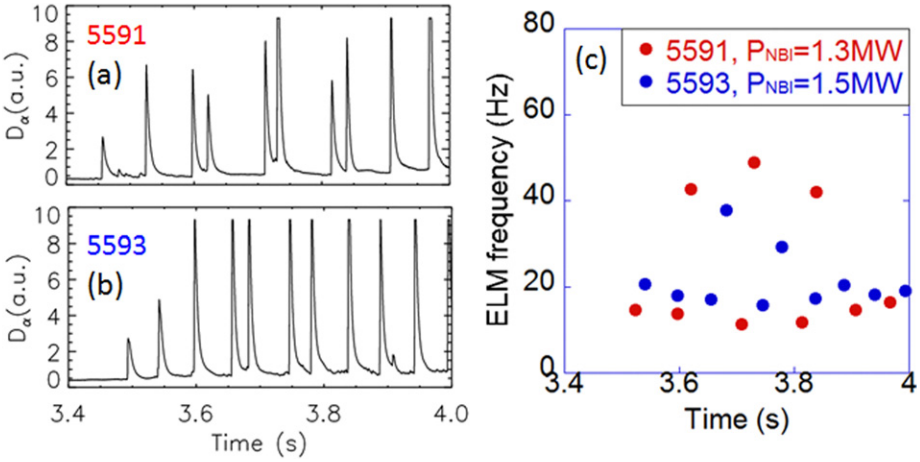

Figure 5. D_α time traces for (*a*) lower and (*b*) higher NBI power discharges. ELM frequency (f_{ELM}) time trace is shown in (*c*) for both cases. The 1.5 MW P_{NBI} shot has a higher ELM frequency than the 1.3 MW case. Note that the outliers at f_{ELM} = 30–50 Hz represent the secondary ELM peaks adjacent to the primary ELM bursts. Thus their frequency is always higher than the primary ELMs and its relationship with the heating power does not reflect the characteristics of primary ELM peaks.

the inter-ELM period for a few tens of ms before the ELM burst (see figure 8(*a*)). This is different from the ELM precursors observed in AUG [24], which only lasted ∼1 ms before the ELM at 15–25 kHz (counter-I_p NBI. No precursor was detected from Mirnov signals for co-I_p), but is similar to the type-I ELM precursor at JET [25], which occurred at ∼20 kHz and had a longer lifetime of 20–30 ms. The intermediate and mixed ELMs do not show precursor events, see figures 8(*b*) and (*c*). The result for intermediate ELMs in KSTAR is not the same as that for type-III ELMs in AUG [24], where precursors at 50–70 kHz (co-I_p) and 80–120 kHz (counter-I_p) were detected by Mirnov coils. Also, the intermediate ELMy H-mode shows a higher level of broadband fluctuation during the inter-ELM period than the other two types of ELMy H-modes. Another thing to note is that the Mirnov signals show an oscillation (300–400 Hz) during the type-I inter-ELM period even though there is nothing detected in the D_α signal. This oscillation and the 25–50 kHz ELM precursor mentioned above generally coexist. The frequency of this oscillation is similar to that of small ELMs in the mixed-ELM regime. We currently do not have a consistent physical picture to explain our observation in comparison with other machines but a detailed mode number analysis and an effort to link it to the ELM stability physics would considerably improve our understanding.

4. Profile measurement during the ELM cycle for type-I ELMy H-mode

A CES diagnostic [13] has been in operation since 2010 and provided T_i and V_t profiles with spatial and temporal resolutions of up to 5 mm and 10 ms, respectively. An interesting feature of these profiles is the presence of a clear pedestal structure during the H-mode, while there is no pedestal for the L-mode plasmas [26]. The temporal evolution of low-field side (LFS) T_i and V_t profiles during an inter-ELM period is shown in figure 9. The V_t profile crashes immediately after the ELM burst but its pedestal quickly begins to increase and the whole profile continues to build up during the period until it crashes again after the next ELM burst. However, the recovery of the T_i pedestal after the crash does not occur until it finally rises back up at the last stage of the inter-ELM period, i.e. >70–80% of the ELM cycle. Figure 10 shows the temporal evolution of pedestal T_i and V_t during the ELM cycle for three

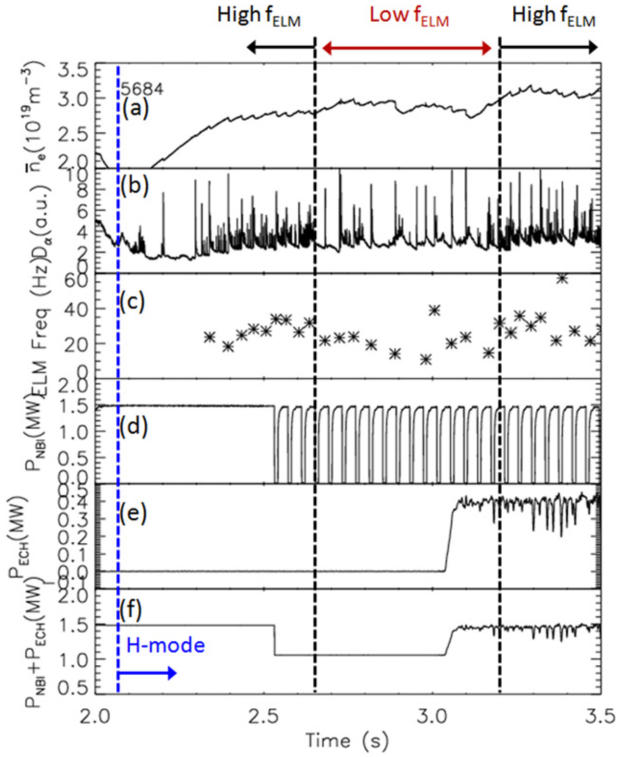

Figure 6. Dependence of ELM frequency on heating power for large ELMs in the mixed-ELM regime. Time traces of (*a*) line average density, (*b*) divertor D_α, (*c*) ELM frequency, (*d*) NBI power (modulated from $t = 2.5$ s), (e) ECH power, and (*f*) total heating power ($P_{\rm NBI} + P_{\rm ECH}$). The NBI modulation from $t = 2.5$ s reduces the NBI heating power to 1.1 MW and the addition of ECH power from $t = 3$ s raises the total auxiliary heating power ($P_{\rm aux} = P_{\rm NBI} + P_{\rm ECH}$) back up to 1.5 MW. The frequency of the large ELMs decreased with lower $P_{\rm NBI}$ with a time delay of ~150 ms and went up again when the total power was raised (see (*c*)). Tiny ELMs between large ELM peaks also disappeared during the lower power phase.

different discharges and the characteristics described above are consistently demonstrated. This result is in contrast to the observation from other machines such as DIII-D [27] that the pedestal height of $T_{\rm i}$ slowly increased throughout the ELM cycle after an initial jump early in the cycle, i.e. within 10–20% of the inter-ELM period. It might also suggest that the ion component of the pressure plays a more important role in the ELM destabilization in KSTAR, but obviously more work is needed to identify specific processes responsible for the ELM stability physics.

Measurement of $T_{\rm e}$ profiles was made by the ECE diagnostic [12], with the absolute calibration of a radiometer system completed for the second and third harmonics of electron cyclotron frequencies for the $B_{\rm t}$ range 1.5–3 T. The present radiometer frequency range 110–162 GHz is optimized for the operation of $B_{\rm t} = 2.5$–3 T, i.e. no harmonics overlap for both the LFS and high-field side (HFS) at 2.5 T and only for the LFS at 3 T. However, KSTAR was operated mostly at $B_{\rm t} = 2$ T in 2011, for which ECE was only able to measure $T_{\rm e}$ for the HFS where the overlap of the second and third harmonics occurs for $r \leqslant 1.54$ m. Therefore the pedestal $T_{\rm e}$ profile could not be obtained even for the HFS side. Fortunately, we had a few higher $B_{\rm t}$ discharges and they allowed ECE to measure more of the LFS $T_{\rm e}$ profile. Figure 11 is an example of such a measurement for the inter-ELM period of a $B_{\rm t} = 2.4$ T H-mode, with and without ECH heating. A significant portion of both the LFS and HFS $T_{\rm e}$ profiles was measured for pure second harmonic frequencies although they still did not quite reach the pedestal region yet. The central $T_{\rm e}$ is 3–4 keV and the whole profile is rather peaked. Although the pedestal $T_{\rm e}$ could not be accurately identified due to the absence of data from $r \sim 2.15$ m, the continuous restoration of the LFS $T_{\rm e}$ profile during the inter-ELM period after the ELM crash is clearly exhibited while the HFS profile only shows a little change. This result is compared with the data from AUG [28], where distinct phases have been observed in the build-up of the pedestal $T_{\rm e}$ profile ($\rho_{\rm pol} > 0.8$). However, the $T_{\rm e}$ profile at $\rho_{\rm pol} = 0.8$ remained almost the same during the entire ELM cycle in this work. Although the ELM $T_{\rm e}$ crash is stronger on LFS than HFS both with and without ECH heating (see figure 11), the discrepancy between the LFS and HFS $T_{\rm e}$ profiles is significantly larger in the case of ECH heating, for which we do not have a good explanation at present. Note that a similar observation of in–out asymmetric $T_{\rm e}$ profiles was reported at JET [29], where cases of different LFS/HFS $T_{\rm e}$ at the same flux surface are presented and the trend of larger ELM $T_{\rm e}$ crashes on the LFS is stronger at higher densities. The underlying mechanism of this asymmetry remains unclear and needs more study to be clarified. Confirmation with the Thomson scattering [30] data in the next campaign and more detailed transport analysis will enable us to unfold the physics responsible for these observed profile changes. If we assume a pedestal $T_{\rm e}$ of ~1 keV from figure 11(*a*) and a pedestal density of $n_{\rm e} \sim (1.5–2) \times 10^{19}\,{\rm m}^{-3}$ from the measured line average density of $\bar{n}_{\rm e} \sim 2.35 \times 10^{19}\,{\rm m}^{-3}$ at $t = 2.4$ s, the neoclassical electron pedestal collisionality, $\nu_{\rm e}^* = q_{95} R \varepsilon^{-1.5} \lambda_{\rm ee}^{-1}$, is estimated to be $\nu_{\rm e}^* \sim 0.5$–0.6. Note that type-I ELMs observed in other tokamaks occurred in a wide range of collisionality, $0.05 \leqslant \nu_{\rm e}^* \leqslant 5$.

5. Characteristics of ELM suppressed H-mode by the applied MPs

KSTAR has recently achieved ELM suppression with $n = 1$ external MPs [14]. It used three rows of in-vessel coils (upper, mid-plane and lower ones) with a generated MP of $\delta B/B = 0.1\%$ with $B_{\rm t} = 2.0$ T at the separatrix. The reference discharge had operation parameters similar to other H-mode shots, i.e. $I_{\rm p} = 0.6$ MA, $B_{\rm t} = 2$ T and $P_{\rm NBI} = 1.3$ MW. The confinement and ELM characteristics for these plasmas are found to be significantly altered after the application of MP. Figure 12 shows the time traces of line average density, mid-plane D_α, and the coil currents for an ELM suppression discharge. It is seen that the electron density begins to fall, i.e. the 'density pump-out stage', as soon as the mid-plane coil current is above a certain value from $t \sim 3.2$ s. Then a short period of density saturation follows after the upper and lower coil currents are turned on at $t \sim 3.3$ s. The density finally begins to increase gradually when all three coil currents reach the full amplitude at $t \sim 3.6$ s and it continues to rise until the H–L back transition occurs at $t = 4.8$ s. The ELM frequency ($f_{\rm ELM}$) suddenly drops and the ELM size ($\Delta\bar{n}_{\rm e}/\bar{n}_{\rm e}$) jumps as

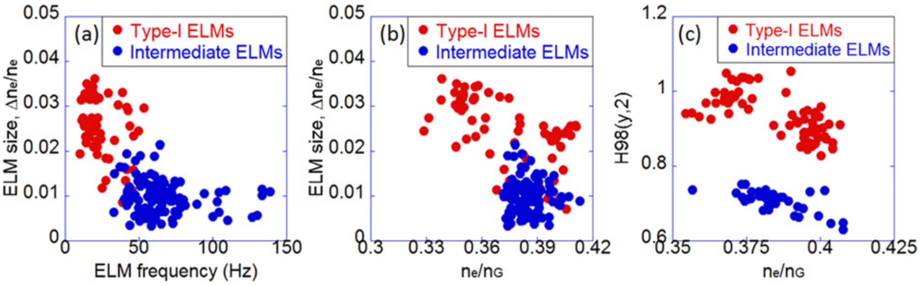

Figure 7. Comparison of type-I (red) and intermediate (blue) ELMs; (*a*) ELM size versus ELM frequency, (*b*) ELM size versus the Greenwald fraction, and (*c*) $H_{98(y,2)}$ versus the Greenwald fraction. (*a*) and (*b*) are for the same time slices. The intermediate ELMy H-mode has a consistently lower H-factor compared with the type-I ELMy. Also, it is apparent that the H-factor decreases with increasing the Greenwald fraction for both ELM types.

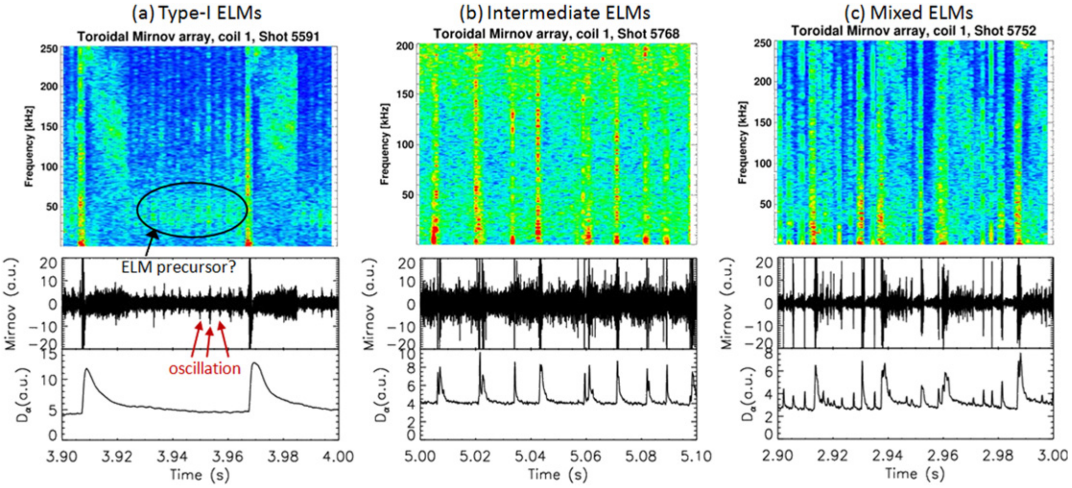

Figure 8. Wavelet analysis of the toroidal Mirnov signal for (*a*) type-I ELMs, (*b*) intermediate ELMs, and (*c*) mixed ELMs. Increased level of fluctuations (ELM precursor) during the inter-ELM period before the ELM burst is observed for type-I ELMs in the 25–50 kHz band and lasts for 40–50 ms.

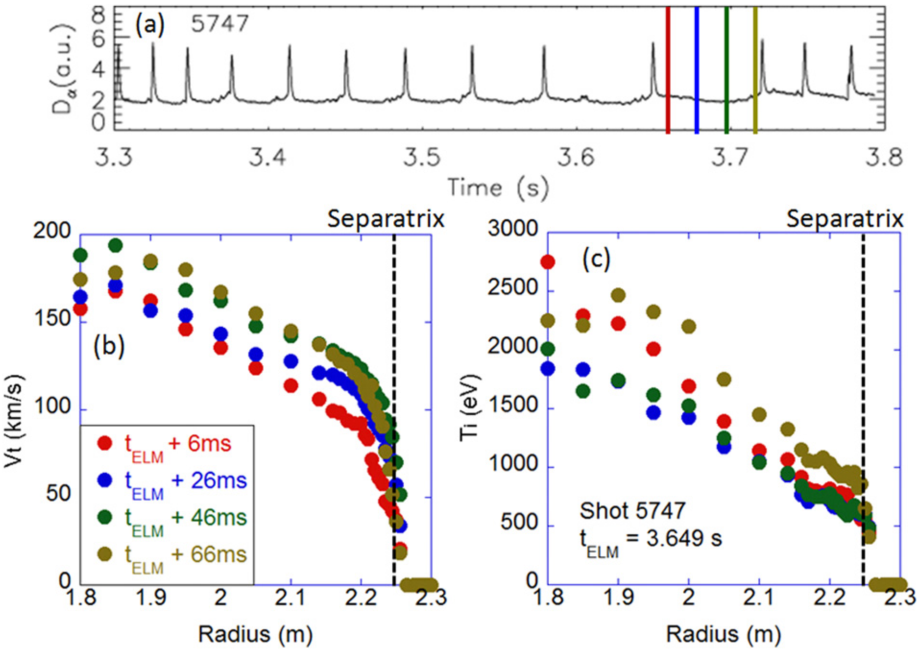

Figure 9. Temporal evolution of (*b*) toroidal velocity (V_t) and (*c*) ion temperature (T_i) profiles during an inter-ELM period of a type-I ELMy H-mode. Four time slices during the inter-ELM period are colour coded. The vertical line represents the radial location of the separatrix from the EFIT reconstruction.

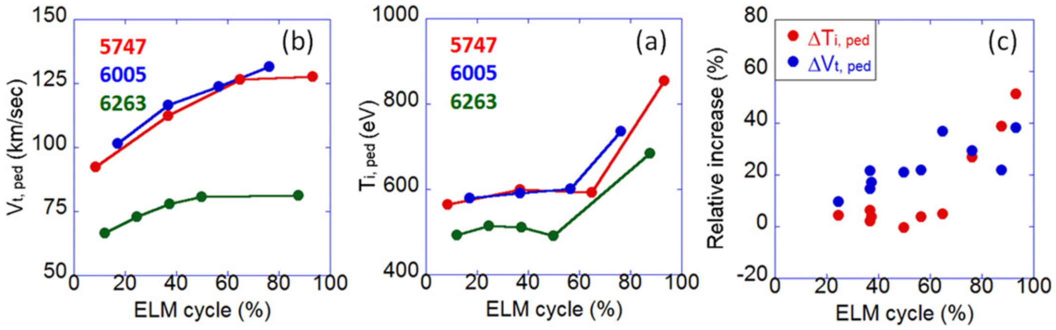

Figure 10. Temporal evolutions of (*a*) pedestal toroidal velocity ($V_{\mathrm{t,ped}}$) and (*b*) pedestal ion temperature ($T_{\mathrm{i,ped}}$) in the ELM cycle for three different discharges. (*c*) shows the relative increase in $V_{\mathrm{t,ped}}$ and $T_{\mathrm{i,ped}}$ with respect to the value at the first time point in each ELM cycle, combined for all three discharges.

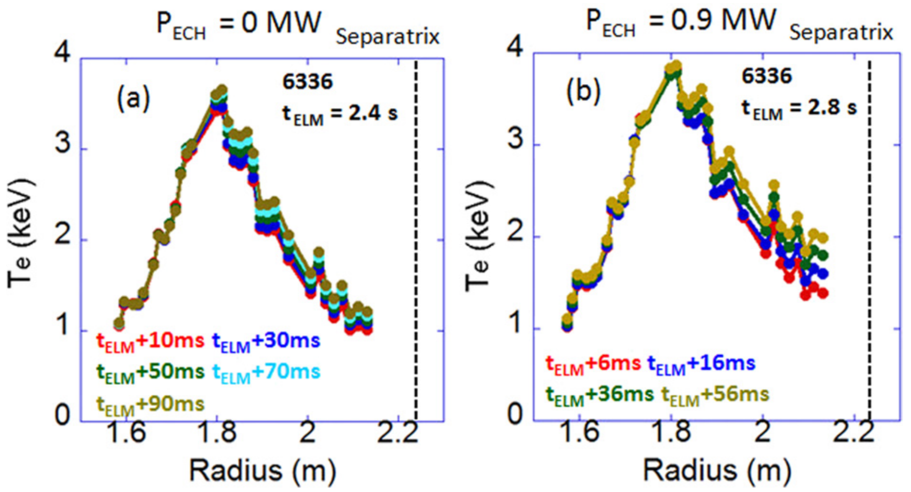

Figure 11. Temporal evolution of T_{e} profile during the inter-ELM period of a type-I ELMy H-mode with $B_{\mathrm{t}} = 2.4\,\mathrm{T}$ and $P_{\mathrm{NBI}} = 1.5\,\mathrm{MW}$, measured by ECE. Four time slices during the inter-ELM period are colour coded. Note that there is very little change in the HFS T_{e} profile. The vertical line represents the radial location of the separatrix from the EFIT reconstruction.

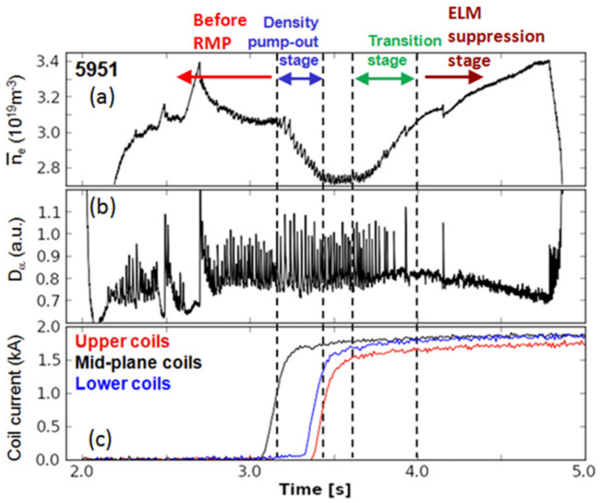

Figure 12. Time traces of (*a*) line average density, (*b*) D_{α} intensity and (*c*) coil currents for an $n = 1$ ELM suppression discharge. The four identified stages are colour coded.

soon as the density pump-out stage begins, i.e. the ELM 'intensification' is initially induced. Then f_{ELM} increases continuously and $\Delta\bar{n}_{\mathrm{e}}/\bar{n}_{\mathrm{e}}$ keeps decreasing during the whole period of the density pump-out stage. After a brief density saturation, a period of decreasing ELM frequency follows, while the electron density goes up, until the ELMs are completely suppressed from $t \sim 4\,\mathrm{s}$. We will call this period ($t = 3.5$–$4.0\,\mathrm{s}$) the 'transition stage'. The ELM size for this period increases slowly in time although the data show substantial scatter. Figure 13 shows the temporal evolution of ELM frequency and size as well as an ELM size versus ELM frequency plot, for which five ELM suppression discharges have been combined in order to improve statistics. Note that the ELM size inversely depends on the ELM frequency for both the density pump-out and transition stages but the relationship is weaker for the transition stage. This is consistent with the observation that the rate of change of $H_{98(y,2)}$ is slower for the transition stage than for the density pump-out stage (see figure 14). The increase in density and H-factor during the transition stage is steady, which suggests that both the particle and energy confinement continues to be enhanced although the enhancement is not as rapid as that for the normal inter-ELM period without the MP application (e.g. period of $t = 2.6$–$2.7\,\mathrm{s}$ in figure 12(*a*)). However, during the ELM suppression stage, the H-factor slightly degrades in time while the density continues to increase. It is interesting to note that the energy confinement quality keeps going down regardless of whether the ELMs are suppressed or not after $t \sim 4\,\mathrm{s}$ (see figure 14). We suspect that modified edge transport by the applied MP is responsible for this change in the

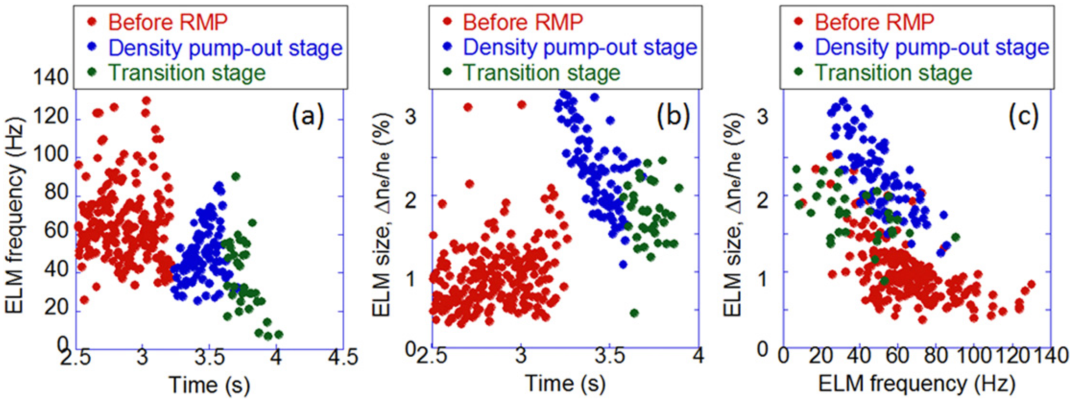

Figure 13. Temporal evolution of (*a*) ELM frequency and (*b*) ELM size for five $n = 1$ ELM suppression discharges. (*c*) is the ELM size versus ELM frequency plot and shows that the inverse proportionality for the transition stage (see figure 12) is substantially weaker than for the density pump-out stage.

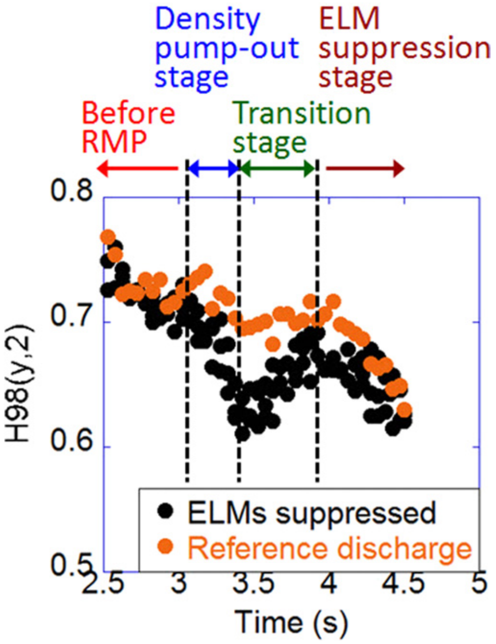

Figure 14. Temporal evolution of the $H_{98(y,2)}$ factor for all stages shown in figure 12 for three $n = 1$ ELM suppression discharges (black) and for a reference discharge without MP (orange). All data are during the H-mode phase.

confinement characteristics but pedestal profile measurements are necessary for a detailed investigation.

It should be mentioned that the determination of the type of ELMs for the MP ELM suppression experiment is yet to be finalized. The ELMs have similar characteristics to those we described for figure 4(*b*) in section 3.3, i.e. higher ELM frequency ($f_{\mathrm{ELM}} = 40$–130 Hz) and lower H-factor ($H_{98(y,2)} = 0.65$–0.75) than for the type-I ELMs. Also, data points for the ELM suppression discharges do not follow the trend for type-I ELMs shown in figures 7(*a*) and (*b*). In fact, data for the intermediate ELMs (blue points) in figure 7 are from the pre-MP phase for a series of MP ELM suppression discharges, but the range of the Greenwald fraction for the dataset is too narrow to deduce a trend as a function of n_e/n_G. One might also suspect from the data in figure 13 that the type of ELMs may have been changed across the beginning of the density pump-out stage, for example from type-III to type-I, with the ELM intensification caused by the application of mid-plane MP. However, the reduction of the H-factor (see figure 14) during the density pump-out stage is not consistent with the characteristic of type-I ELMy H-modes. We therefore would like to leave the possibility open for the ELM types before and after the MP application for the ELM suppression experiment. An NBI power scan is planned in the coming campaign to examine the ELM frequency dependence to clarify this issue.

6. Plasma control and access to the late H-mode

A typical H-mode discharge in KSTAR has an L–H transition at $t = 2$–3 s, the H-mode state lasting for a few seconds, then an H–L back transition takes the plasma back to the L-mode state and it continues until the plasma consumes all of the available flux. However, we have observed a second L–H transition at a later stage of some H-mode discharges (see figure 1). The H–L back transitions from the main H-mode and the access to this late H-mode appear to be caused by the loss and re-gain of the plasma control, respectively. The KSTAR plasma control system currently does not have a feedback loop to control the plasma shape, and the H-mode only lasts as long as the divertor configuration is properly maintained and the inner separatrix is detached from the inner wall. When the plasma shaping becomes weak after a while (typically in a few seconds after the first L–H transition), the divertor configuration is significantly relaxed and the inner separatrix hits the wall. This typically triggers the H–L back transition immediately or shortly afterwards. Then the L-mode stage lasts for a while but the feed-forward plasma control is still in action and can sometimes restore the divertor configuration when the L-mode state lasts long enough and an appropriate plasma condition is combined with the plasma control. In this case, the inner separatrix gets detached from the wall again and the second L–H transition (late H-mode) is triggered. Figure 15 shows the plasma cross section from the EFIT equilibrium reconstruction for both the main and late H-mode phases for the same discharge in figure 1. The plasma configuration is close to double null divertor (DND) with dr_{sep} around −5 mm for both the main and late H-mode states, but

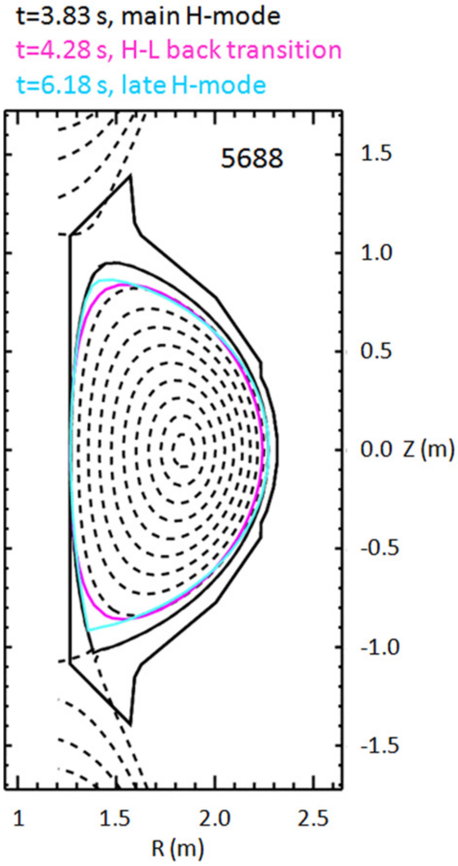

Figure 15. Poloidal cross section of the plasma from the EFIT equilibrium reconstruction for (a) main H-mode (type-I ELMy), (b) near the H–L back transition from the main H-mode, and (c) late H-mode (mixed ELMy) phases.

the plasma elongation at the L–H transition time is noticeably lower ($\kappa = 1.6$–1.7) for the late H-mode than for the main H-mode ($\kappa = 1.8$–1.9). Also, the X-point location for the late H-mode phase is slightly closer to the inner wall and this makes, along with the lower κ the plasma cross section more triangular and thus δ is higher ($\delta \sim 0.8$) than for the main H-mode ($\delta \sim 0.6$). For the discharges in this study, the late H-mode plasmas have densities in a substantially wider range of the Greenwald fraction ($0.38 \leqslant (\bar{n}_e/n_G) \leqslant 0.57$), while densities in the preceding main H-mode were in a narrower range ($0.36 \leqslant (\bar{n}_e/n_G) \leqslant 0.42$). Among the plasma parameter changes, the T_i and V_t increases induced by the transition to the late H-mode are significantly lower than those for the main H-mode.

The late H-mode also has different ELM characteristics from the main H-mode and we suspect this may be due to the shaping parameter change described above, i.e. lower κ and higher δ. Figure 16 shows time traces of density and D_α for the main and late H-mode stages for shot 5687. It is seen that the main H-mode ELMs primarily have clear and large D_α spikes but the late H-mode shows a mixture of large type-I ELMs and tiny ELM peaks. The size and frequency of large ELMs for the main and late H-mode is usually up to 3–4% of $\Delta\bar{n}_e/\bar{n}_e$ and $f_{ELM} = 10$–60 Hz, while the late H-mode small ELMs have size below ~0.5% and frequency up to ~260 Hz. Figures 17(*a*) and (*b*) show the plots of ELM size versus frequency for all three categories of ELM described above. The first thing to note is that the size of large ELMs for the main H-mode decreases with increasing ELM frequency but those for the late H-mode show a large scatter. On the other hand, small ELMs for the late H-mode reveal no correlation between the size and frequency. The confinement quality of the late H-modes is as good as or above that of the main H-modes. Figure 17(*c*) compares $H_{98(y,2)}$ for the main H-phase to that for the late H-phase. The H-factor for the late H-mode is rather flat, $H_{98(y,2)} = 0.9$–1.1, even with the wider range of the Greenwald fraction ($0.45 \leqslant (\bar{n}_e/n_G) \leqslant 0.6$) than for the main H-mode ($0.35 \leqslant (\bar{n}_e/n_G) \leqslant 0.4$). Note that the H-factor for the main H-mode decreases from ~1.1 to ~0.8 with increasing Greenwald fraction as seen for type-I ELMs in figure 7(*c*).

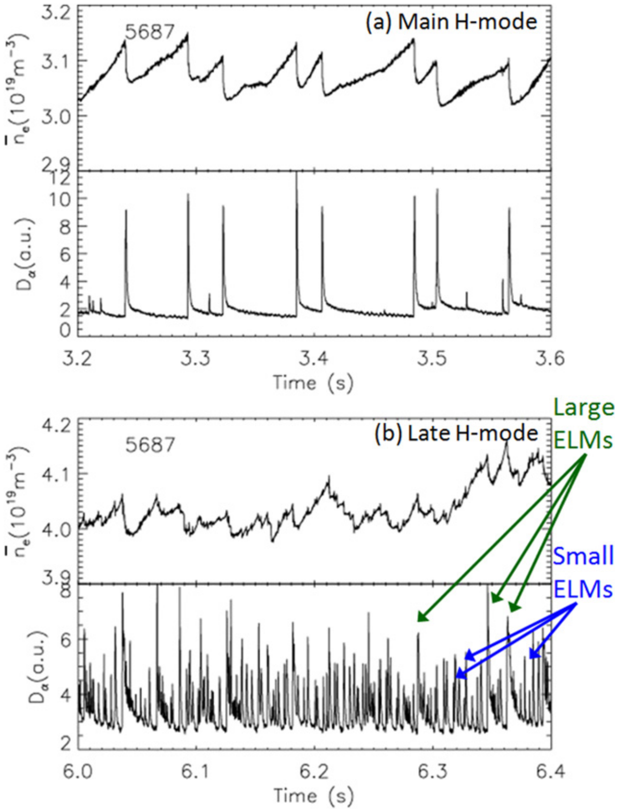

Figure 16. Line average density and D_α traces for (*a*) main H-mode and (*b*) late H-mode stages for shot 5687. Note that the late H-mode is in a mixed-ELM regime.

7. Summary and conclusions

The fast ion component of the stored energy is calculated by NUBEAM and ASTRA and is subtracted from the total stored energy computed by EFIT. The fraction of W_{fast} rapidly increases with decreasing density. This makes the accurate estimation of W_{fast} more important in the lower density regime for the evaluation of thermal energy confinement time. The L–H power threshold study reveals a roll-over of P_{thr} with minimum at $\bar{n}_e \sim 2 \times 10^{19}\,m^{-3}$. However, for densities above $2 \times 10^{19}\,m^{-3}$, the evaluated P_{thr} agrees well with the prediction from the multi-machine scaling law. KSTAR ELMs appear to be categorized as three distinctive types: large type-I ELMs with low frequency and big ELM size with

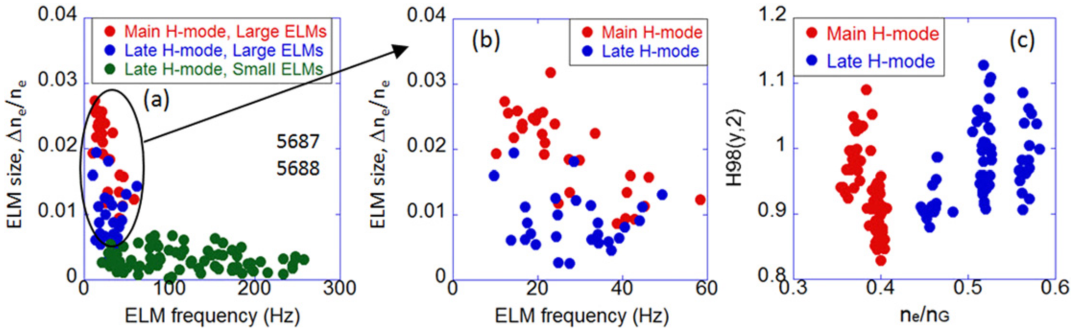

Figure 17. (*a*) ELM size versus ELM frequency plot for large ELMs in main (red) and late (blue) H-modes, and for small ELMs in late H-mode (green). (*b*) is an enlarged version of the same plot for large ELMs in (*a*). (*c*) is the $H_{98(y,2)}$ versus the Greenwald fraction plot for main (red) and late (blue) H-mode phases. This is for the same discharges for (*a*) and (*b*) but the averaging time window is different.

good confinement; intermediate ELMs with higher frequency and poorer confinement; mixed ELMs with large and small peaks with good confinement. Preliminary power scan data showed that the frequency of large ELM peaks for the type-I and mixed-ELM regimes has a positive dependence on the heating power, a typical feature of type-I ELMs. The ELM size of intermediate ELMs is not correlated with either the ELM frequency or the Greenwald fraction, while it inversely depends on both quantities for type-I ELMs. We suspect the intermediate ELMs might be type-III because of their size and frequency characteristics distinctive from type-I ELMs and the poorer confinement quality. Mirnov signals show an increased fluctuation level in the low-frequency band (25–50 kHz) along with 300–400 Hz of oscillation during the inter-ELM period for type-I ELMy H-mode, while there is no precursor signal for the intermediate and mixed ELMs. Profile measurements during an ELM cycle indicate that the T_i pedestal only jumps in the last stage (after 70–80% of the ELM cycle) whereas the T_e and V_t pedestals steadily rise over the entire ELM cycle. This suggests that the ion component of the pressure might be more responsible for the ELM destabilization in KSTAR. The ELM suppressed H-mode discharges exhibit three distinctive stages during the application of magnetic perturbations: density pump-out stage, transition stage and ELM suppression stage. The confinement and ELM characteristics show very dynamic changes over the course of the three stages. The H-factor rapidly decreases during the density pump-out stage and rises back up slowly during the transition stage until it finally reaches saturation and slightly degrades in time. The H-factor during the ELM suppression stage continues to decrease similarly to the reference case with ELMs. ELMs initially show strong intensification with the beginning of the density pump-out stage but the ELM size (frequency) rapidly drops (grows) in time until the plasma reaches the transition stage, during which the ELM frequency quickly decreases but the ELM size only gradually increases. The cause of the late L–H transitions is thought to be the restoration of plasma shaping, i.e. divertor configuration, and the detachment of the inner separatrix from the wall. Only the mixed-ELM regime appears during the late H-mode stage and the change in shaping parameters, i.e. lower κ and higher δhan for the main H-mode, appears to be related to the change in ELM characteristics. Small ELMs between large ELM peaks in the mixed-ELM regime have very different characteristics, i.e. tiny ELM size and no size dependence on the ELM frequency.

Acknowledgments

The authors are grateful to Dr R. Maingi, Oak Ridge National Laboratory, for helpful discussion and suggestions. This work was supported by the Korea Ministry of Education, Science and Technology (MEST). J-W. Ahn and D.L. Hillis acknowledge the support of the Oak Ridge National Laboratory managed by UT-Battelle, LLC for the US Department of Energy under contract no DE-AC05-00OR22725. Part of the work was also supported by National R&D Programme through the National Research Foundation of Korea funded by the Korean government (MEST), contract nos 2011-0018731 and 2012-0000590.

References

[1] Lee G.S. *et al* 2000 *Nucl. Fusion* **40** 575
[2] Kwon M. *et al* 2011 *Nucl. Fusion* **51** 094006
[3] Yoon S.W. *et al* 2011 *Nucl. Fusion* **51** 113009
[4] Sartori R. *et al* 2004 *Plasma Phys. Control. Fusion* **46** 723
[5] Nam Y.U. *et al* 2008 *Rev. Sci. Instrum.* **79** 10E705
[6] Ryter F. *et al* 2009 *Nucl. Fusion* **49** 062003
[7] Fukuda T. *et al* 2000 *Plasma Phys. Control. Fusion* **42** A289
[8] Maggi C.F. *et al* 2011 L–H threshold at low density and low momentum input in the JET tokamak *Proc. 38th EPS Conf. on Plasma Physics (Strasbourg, France, 2011)* P4.061 http://ocs.ciemat.es/EPS2011PAP/pdf/P4.061.pdf
[9] Xu G.S. *et al* 2011 *Nucl. Fusion* **51** 072001
[10] Martin Y.R. *et al* 2008 *J. Phys.: Conf. Ser.* **123** 012033
[11] Fundamenski W. *et al* 2012 *Nucl. Fusion* **52** 062003
[12] Jeong S.H. *et al* 2010 *Rev. Sci. Instrum.* **81** 10D922
[13] Ko W.H. *et al* 2010 *Rev. Sci. Instrum.* **81** 10D740
[14] Jeon Y.M. *et al* 2012 *Phys. Rev. Lett.* **109** 035004
[15] Park Y.S. *et al* 2011 *Nucl. Fusion* **51** 053001
[16] Polevoi A. *et al* 1997 JAERI-Data/Code 97–014
[17] Pereverzev G.V. *et al* 2002 *IPP Report* 5/98, Max-Planck Institut für Plasmaphysik
[18] Goldston R.J. *et al* 1981 *J. Comput. Phys.* **43** 61
[19] Pankin A. *et al* 2004 *Comput. Phys. Commun.* **159** 157
[20] ITER Physics Expert Groups in Confinement and Transport 1999 ITER Physics Basis Chapter 2: Plasma confinement and transport *Nucl. Fusion* **39** 2175
[21] Zohm H. *et al* 1996 *Plasma Phys. Control. Fusion* **38** 105
[22] Loarte A. *et al* 2003 *Plasma Phys. Control. Fusion* **45** 1549
[23] Urano H. *et al* 2003 *Plasma Phys. Control. Fusion* **45** 1571
[24] Kass T. *et al* 1998 *Nucl. Fusion* **38** 111
[25] Poli F. *et al* 2008 *Plasma Phys. Control. Fusion* **50** 095009
[26] Ko W.H. *et al* 2011 The behaviors of the ion temperature and impurity rotation profiles from charge exchange spectroscopy during H-mode in KSTAR *Bulletin of the*

53rd APS-DPP Annual Meeting (Salt Lake City, UT 2011) TP9.00139 http://meetings.aps.org/Meeting/DPP11/Event/153252

[27] Groebner R.J. *et al* 2009 *Nucl. Fusion* **49** 045013

[28] Burckhart A. *et al* 2010 *Plasma Phys. Control. Fusion* **52** 105010

[29] de la Luna E. *et al* 2007 Measurements of inboard-outboard asymmetry of pedestal temperature collapse during Type I ELMs in JET *Proc. 34th EPS Conf. on Plasma Physics (Warsaw, Poland, 2007)* P5.085 http://epsppd.epfl.ch/Warsaw/pdf/P5_085.pdf

[30] Lee J.H. *et al* 2010 *Rev. Sci. Instrum.* **81** 10D528